COMMUNICATIONS MATERIALS

ARTICLE

https://doi.org/10.1038/s43246-019-0006-5 OPEN

Hydrodynamic inflation of ring polymers under shear

Maximilian Liebetreu[1]* & Christos N. Likos[1]*

Hydrodynamic interactions can dramatically influence the dynamics of fully flexible, ring-shaped polymers in ways unknown for any other polymer architecture or topology. Tumbling under shear is a common dynamic pattern of motion for all polymer architectures. Here we show the existence of a shear-induced inflation phase exclusive to ring polymers, the onset of which depends on the ring's contour length. This is accompanied by a strong suppression of tumbling, which resumes at even higher shear rates. The ring swells in the vorticity direction, and the horseshoe regions on the stretched and swollen ring are effectively locked in place relative to its center-of-mass. Furthermore, knots tied onto such rings can serve as additional 'stabilisation anchors'. Under strong shear, the knotted section remains well-localised while tank-treading from one horseshoe region to the other in sudden bursts. We find knotted polymers of high contour length behave very similarly to unknotted rings of the same contour length.

---

[1] Faculty of Physics, University of Vienna, Boltzmanngasse 5, A-1090 Vienna, Austria. *email: maximilian.liebetreu@univie.ac.at; christos.likos@univie.ac.at

The influence of topology on the physical properties of macromolecules is profound and manyfold[1]. The most striking manifestation of this fact is the vast richness of novel phenomena emerging in the behaviour of ring polymers, both at the single-molecule level as well as for concentrated solutions and melts[2–6]. Of immediate interest is, for example, the interplay between molecular architecture, deformation and dynamics under shear, but also how these affect stress distribution, viscosity, rheology and thixotropic behaviour of sheared concentrated solutions. The conformations of single molecules and the ensuing effective interactions[7–9], the self-organisation of concentrated ring polymer solutions and melts[10–14], the viscosity and stress relaxation under shear[5,15–17] as well as the possibility of emergence of novel, topologically glassy states for ring polymer melts[18,19] are a few characteristic examples of the variety of properties unique to cyclic polymers. Concomitantly, the out-of-equilibrium behaviour of rings under tailored microfluidic flows has also attracted considerable attention in the recent past[20–23].

As the probability to obtain unknotted polymers decreases exponentially with their contour length[24], the importance of knots on polymer behaviour is an additional topic of intensive research activity. Knots are naturally found on long DNA strands[25–27] and proteins[28–30], while at the same time they can also be artificially[31,32] or synthetically manufactured[33]. The influence of such knots in equilibrium and relaxation properties in the bulk[34,35], under confinement[36,37] and under tension[38–42] has been thoroughly investigated. Recently, the sedimentation behaviour of flexible, non-Brownian knots has been added to the host of counterintuitive phenomena[43].

All polymer architectures (linear, star, dendritic, cross-linked and ring) are known to undergo tumbling under steady shear at sufficiently high shear rates[22,44–47]. Moreover, it is known that linear chains never fully stretch under shear and they reach a stretched configuration only under so-called planar mixed flows that represent a combination of simple shear and planar extension[23,48,49]. Under simple shear, ring polymers show two dynamical modes: tumbling (TB) and tank treading (TT)[50]. During TB, the polymer's shape changes rapidly as the ring collapses and expands again, with beads at the horseshoe regions swapping to the opposite side. The transition between the initial and final state can best be described by the flipping of a disc, except it collapses onto itself during the flipping procedure. TT, on the other hand, is vastly different and becomes pronounced for stiff rings: the polymer ring maintains its shape, but beads start moving along its shape around the vorticity axis. This can best be visualised by a coin rolling on its edge, or the wheels of a tank.

In previous work, we have highlighted the importance of fully developed hydrodynamics when investigating ring polymers under shear[22]. Through a coupling between hydrodynamic interactions (HI) and topology unique to the ring architecture, circular polymers under shear have been shown to swell in the vorticity direction, a phenomenon that is absent for linear chains and it also disappears for circular polymers when HI is switched off[22,51,52].

Here, we present the emergence of an inflationary phase for longer ring polymers under simple, pure shear and fully developed hydrodynamics caused by a backflow from the horseshoe regions. In this phase, the ring undergoes full unfolding in all directions and transforms itself to an almost rigid, stretched, non-Brownian particle, in which not only TT but also TB motions are suppressed. The inflated regime is unique to ring polymers, but independent of the presence of knots along their backbone, but it requires a minimum polymer size to manifest itself. The aim of this work is to bring forward a novel-type behaviour of rings with and without knots, and to quantify and explain the interplay between HI and topology. We suggest that the swelling of the polymer in vorticity direction might potentially pave the way to distinguishing rings and chains of different sizes, and that shear could be used to reliably tighten knots on rings to unify the behaviour of polymer melts. The vorticity swelling of all rings and its massive impact on dynamics and shape underlines the importance of fully developed HI when studying such polymers in solution, a property we demonstrate additionally by performing simulations without HI and showing that the inflated phase disappears in that case.

We have employed Molecular Dynamics (MD) simulation coupled to a Multi-Particle Collision Dynamics (MPCD) solvent[53], together with Lees–Edwards boundary conditions[54], to simulate a variety of single-ring polymers of various sizes and topologies under shear. In what follows, N stands for the number of beads in the polymer; the topologies simulated were the unknot, 0_1, as well as the prime knots 3_1, 4_1, 5_1, 5_2, 6_1, 6_2, 6_3, 7_1 and 8_1, employing the Alexander–Briggs notation[55] to characterise the knots.

Results

Self-stabilisation of long rings under shear and strong suppression of tumbling. Contrary to open-ended topologies like chains and stars, hydrodynamic interactions on rings cause the polymer to swell not only in flow but also in the vorticity direction[22]. To quantify the polymer's conformation under shear, we consider the gyration tensor[56]

$$G_{\alpha\beta} = \frac{1}{N}\sum_{i=1}^{N}\langle \mathbf{s}_{i,\alpha}\mathbf{s}_{i,\beta}\rangle, \tag{1}$$

where $\mathbf{s}_{i,\alpha}$ is the α-coordinate of particle i's position relative to the polymer's centre-of-mass $\bar{\mathbf{r}}$, such that $\mathbf{s}_i = \mathbf{r}_i - \bar{\mathbf{r}}$ and the symbol $\langle\cdots\rangle$ denotes the expectation value arising from performing an averaging over time. The diagonal elements of this tensor express the polymer's extension in these directions and are shown in Fig. 1, plotted against increasing shear rate $\dot{\gamma}$. With the help of the results in Supplementary Table 1, it can be established that we have reached, for all polymers considered, Weissenberg numbers of order 10^3, well into the strongly nonlinear regime, $Wi \gg 1$.

In flow direction (Fig. 1a, d), G_{xx} increases steadily up to a certain shear rate of $\dot{\gamma} \sim 0.1$ and then it starts decreasing. Along the vorticity direction (Fig. 1b, e), G_{zz} experiences a short decrease and then increases rapidly up to a maximum before decreasing again. This effect is caused by backflow from the horseshoe regions of a stretched ring under shear and is exclusive to the ring topology[22]. Already this non-monotonic behaviour of the vorticity direction diagonal component of the gyration tensor is quite unusual and unique to ring polymers. For linear chains, the back-flowing solvent from the ends that escapes in the vorticity direction does not encounter any monomers there and thus it does not couple to the polymer. Thus, for linear chains, with or without HI, no vorticity swelling takes place, as demonstrated in ref. [22] and shown again here exemplarily for $N = 75$ chains in Fig. 1g–i. We provide Supplementary Movies 1–2 of linear chains that show their typical conformations under shear.

Even more spectacular features show up in the gradient direction diagonal element G_{yy}, shown in Fig. 1c, f. Contrary to all other known polymer types, which display a monotonic decrease of G_{yy} with the shear rate $\dot{\gamma}$, a swelling anomaly shows up for rings, resulting, for sufficiently long rings, in a non-monotonic behaviour of G_{yy} and featuring a local minimum, a rise to a local maximum and a further decrease of this quantity thereafter. The effect is almost invisible for a contour length of $N = 100$, i.e., one needs sufficiently long rings to clearly identify it.

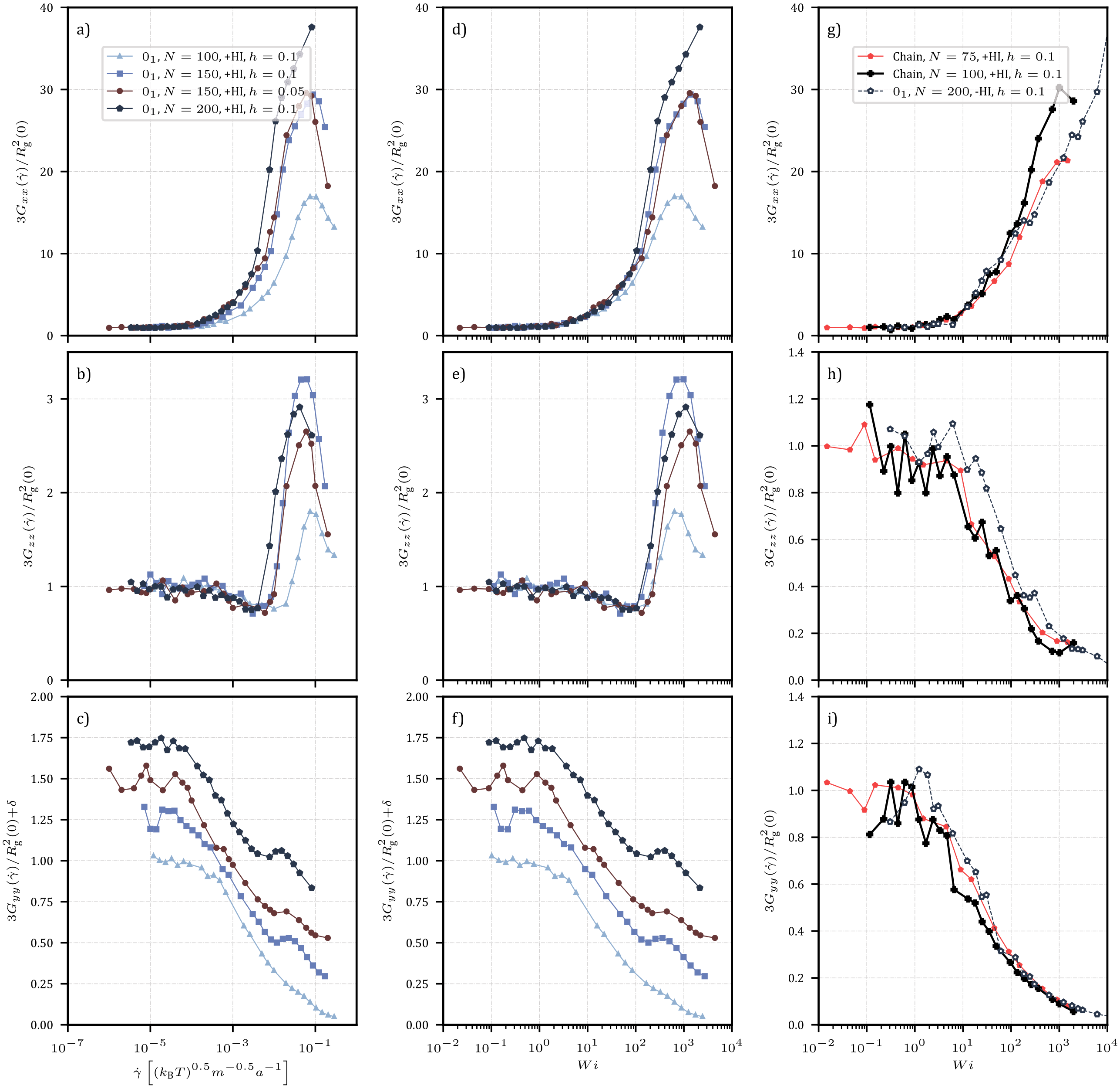

Fig. 1 Diagonal components of the gyration tensor. a–f Diagonal gyration tensor elements $G_{\alpha\alpha}(\dot{\gamma})$ for a set of rings, normalised over their equilibrium value $R_g^2(0)/3$ where R_g is the radius of gyration, against the shear rate $\dot{\gamma}$ in panels **a**–**c** and against Weissenberg number *Wi* in panels **d**–**f**. A more complete discussion of gyration tensor G and the values obtained from it can be found in the Supplementary Methods. **g**–**i** Diagonal gyration tensor elements $G_{\alpha\alpha}(\dot{\gamma})$ for a set of chains including HI and the $N = 200$-ring without HI for reference, normalised over their equilibrium value $R_g^2(0)/3$ where R_g is the radius of gyration, against Weissenberg number *Wi*. **a** G_{xx} (flow direction) increases with shear rate to some maximum and then drops as rings align into the flow–vorticity plane and experience less strain. **b** G_{zz} (vorticity direction) decreases to a minimum and then shoots up at values of $\dot{\gamma}$ that anticipate the inflation anomaly observed in panel **c** for the gradient direction. **c** G_{yy} (gradient direction) initially decreases with shear rate. For $N = 150$ and $N = 200$, an inflation anomaly is observed, which is hardly visible for $N = 100$. The same anomaly is reproduced for MPCD collision time step $h = 0.05$ for the $N = 150$-ring. To highlight this behaviour, shifts δ have been applied along the vertical axis, where $\delta_{N=100} = 0.0$, $\delta_{N=150} = 0.25$ ($h = 0.1$), $\delta_{N=150} = 0.5$ ($h = 0.05$) and $\delta_{N=200} = 0.75$. **g** G_{xx} (flow direction) increases with shear rate and eventually saturates for chains. Saturation was not yet reached for the $N = 200$-ring without HI. **h** G_{zz} (vorticity direction) decreases continuously. The anomaly of rings with HI presented in panels **b** and **e** is absent here. **i** G_{yy} (gradient direction) decreases with shear rate. As the anomaly in panels **c** and **f** is not shown by chains nor rings without HI, no shift was applied to these data.

During the anomaly in the behaviour of G_{yy}, the $N = 150$ and $N = 200$ rings undergo a shift in their typical dynamical patterns, transitioning from the usual motion that features strong thermal fluctuations on the monomer scale, as well as tumbling of the whole macromolecule, towards a new phase in which the ring is stretched and unfolded, and the tumbling motion stops almost completely. At the end of this phase, which takes place for shear rates bracketed by the local minimum and the local maximum of G_{yy}, the ring behaves as a non-Brownian particle for which thermal fluctuations are strongly suppressed by the strong hydrodynamic and elastic forces between connected monomers. More precise estimates of the crossover values of the shear rate to this phase will be determined using the orientational resistance, see Fig. 2c. Since this phase manifests itself as an unfolding of the

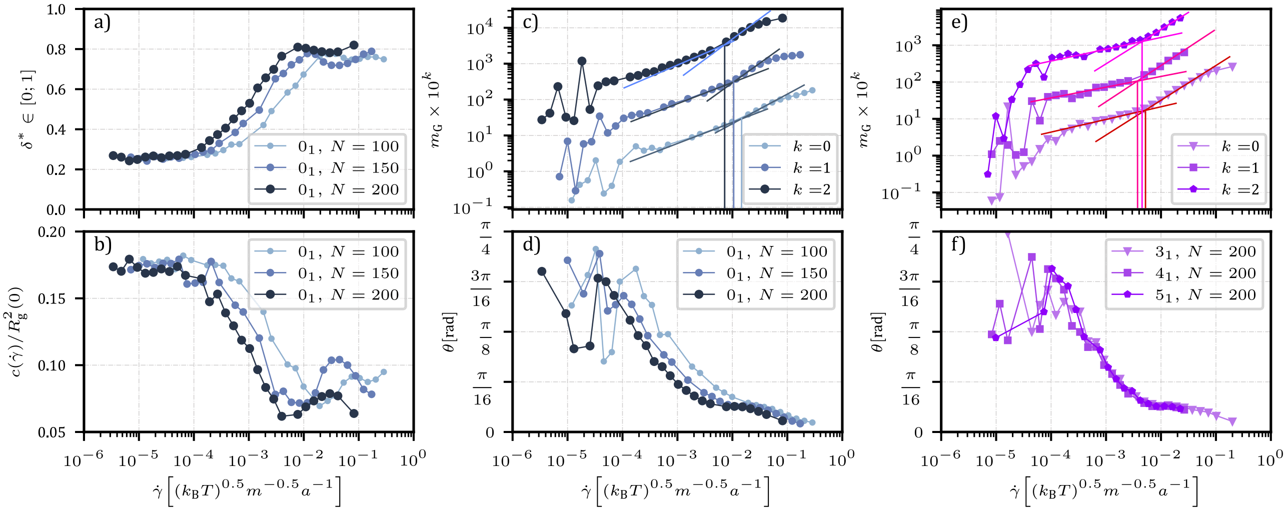

Fig. 2 Shape and orientation of knotted and unknotted ring polymers under increasing shear rate. a Anisotropy δ^*. **b** Acylindricity $c(\dot\gamma)$ scaled over the squared gyration radius at $\dot\gamma = 0$. **c** Orientational resistance m_G for three different 0_1 rings, as denoted in the label of panel **d**. The vertical lines denote crossovers from the tumbling regime at the lower values of $\dot\gamma$ to the inflation regime at higher ones. The straight lines on the left of the crossover have slope 0.6 and the ones on the right have slope 0.85 for $N = 100$ and unity for $N = 150$ and $N = 200$. Curves have been multiplied by constants, providing vertical shifts as indicated in the label. **d** Alignment angle θ between the eigenvector corresponding to the largest eigenvalue of the gyration tensor and the flow axis for the three 0_1 rings. **e** Orientational resistance m_G for three different knotted rings of topologies as denoted in the label of panel **f**. The straight lines on the left of the crossover points have slope 0.6, and the ones on the right have slope unity. The curves have been multiplied by constants, whose values are given in the label, for visual clarity. **f** Same as panel **d**, but for the three knotted rings whose characteristics are summarised in the label.

polymer and a uniform expansion in all directions whilst the ring orientation in space remains fixed (see below) we term it ‘inflation phase’, induced by shear and hydrodynamics. After the development of the inflation phase, the ring becomes fully inflated or stretched. The emergence of this phase requires both the ring topology and the presence of HI. Indeed, as shown in Fig. 1g–i, linear chains with or without HI and cyclic polymers without HI all show normal, monotonic behaviour of the diagonal elements $G_{\alpha\alpha}$ on Wi. We provide Supplementary Movies 3–4 from a $N = 200$-ring under shear without HI to be compared with our additional Supplementary Movies 5–14 of rings under shear with HI taken into consideration.

Very recently, Young et al.[23] applied Brownian Dynamics simulations of chains and rings in mixed planar flows that combine shear with extension, expressed by a relationship of the form $\mathbf{v}_s(\mathbf{r}) = \tilde{\boldsymbol{\Gamma}} \cdot \mathbf{r}$ between solvent velocity and position vector in Cartesian coordinates and the velocity gradient tensor $\tilde{\boldsymbol{\Gamma}}$ having the form

$$\tilde{\boldsymbol{\Gamma}} = \dot\gamma \begin{bmatrix} 0 & 1 & 0 \\ \alpha & 0 & 0 \\ 0 & 0 & 0 \end{bmatrix}. \qquad (2)$$

In ref. [23], the effects of hydrodynamics were accounted for via the Rotne–Prager–Yamakawa (RPY) mobility tensor. The inflation phase and the stretched configurations are absent in their findings for pure shear, corresponding to the value $\alpha = 0$ of the velocity gradient tensor $\tilde{\boldsymbol{\Gamma}}$ above[23,48,49]; interestingly, inflated-like phases are reported in ref. [23] for values $\alpha \neq 0$. The absence of this phase in the aforementioned work could be a consequence of approximating hydrodynamics via the RPY tensor, but it is most likely an effect of the low degree of polymerisation, $N = 120$, employed by Young et al. Further differences with ref. [23] pertain to the solvent quality (θ solvent in ref. [23] vs. good-quality solvent here) and to the modelling of the bonding interactions between the monomers (harmonic vs. FENE springs, respectively).

The shape parameters[44,56], defined mathematically in the Supplementary Methods, are also featuring anomalous behaviour. Two of them, the anisotropy δ^* and the acylindricity c are shown as representatives in Fig. 2a, b. Indeed, the non-monotonic behaviour of the elements of the gyration tensor is directly reflected in similar non-monotonic trends for the aforementioned quantities. Very informative is the behaviour of the orientational resistance $m_G = Wi\ \tan(2\theta)$ and of the alignment angle θ of the polymer with the flow axis, shown in Fig. 2c, d, offering a direct quantitative measure of the onset and the characteristics of the inflation phase. It can be seen that m_G shows a crossover from the usual, $m_G \sim \dot\gamma^{0.6}$ behaviour to a much sharper, $m_G \sim \dot\gamma$ power law, which allows us to define a characteristic crossover shear rate $\dot\gamma_\times$ marked by the vertical lines in Fig. 2c, and summarised in Table 1. The second regime immediately implies that the orientation angle θ does not change with the shear rate $\dot\gamma$, see also the Discussion section below. Moreover, as a direct comparison between Figs. 1c, 2c, d shows, the regime between the local minimum and the local maximum of $G_{yy}(\dot\gamma)$ coincides with the regime of the $m_G \sim \dot\gamma$ scaling, in which the orientation angle θ remains constant and the ring thus merely unfolds, growing in all directions—precisely the inflation phase mentioned above. This scaling lasts for about one decade in $\dot\gamma$, beyond which the slope of m_G becomes again smaller and the tilt angle starts decreasing again with the shear rate. At this stage, inflation is complete and the ring is fully stretched, tilting closer to the flow axis as $\dot\gamma$ grows further. Figure 2e, f show that the same scenario also holds for some selected knotted topologies, to which we will return in the next section.

To further describe, analyse and understand shear-induced ring polymer inflation, we take a closer look at the $N = 150$ and $N = 200$ rings as an example, and compare Supplementary Movies 7–14.

In the tumbling regime: At $\dot\gamma \cong 2.5 \times 10^{-3}$, G_{yy} first reaches the value of the anomaly maximum. We observe the formation of a tilting axis along which the polymer stretches. Tumbling frequently occurs and takes up substantial space in gradient

Table 1 Crossover shear rates $\dot{\gamma}_\times$ and Weissenberg numbers $Wi_\times$ from tumbling to inflation phase.

Topology	N	$\dot{\gamma}_\times$ $[(k_BT)^{0.5}m^{-0.5}a^{-1}]$	$Wi_\times$
0_1	100	1.4×10^{-2}	1.19×10^{2}
0_1	150	1.0×10^{-2}	1.57×10^{2}
0_1	200	7.2×10^{-3}	1.86×10^{2}
3_1	100	1.3×10^{-2}	0.66×10^{2}
3_1	200	5.2×10^{-3}	0.82×10^{2}
4_1	200	3.8×10^{-3}	0.52×10^{2}
5_1	200	4.5×10^{-3}	0.59×10^{2}
5_2	200	6.2×10^{-3}	0.62×10^{2}
6_1	200	6.6×10^{-3}	0.88×10^{2}
6_2	200	7.2×10^{-3}	0.86×10^{2}
6_3	200	6.4×10^{-3}	0.74×10^{2}
7_1	200	7.7×10^{-3}	1.05×10^{2}
8_1	200	7.9×10^{-3}	0.90×10^{2}

The crossover values $\dot{\gamma}_\times$ and $Wi_\times$ for the transition from the tumbling to the inflation phase of ring polymers with topology denoted in the left column and degree of polymerisation N in the second-to-left. Note that for the cases of $N = 100$ (0_1- and 3_1-rings), a fully developed inflation phase does not emerge and $\dot{\gamma}_\times$ denotes the crossover value between the two power-law regimes in Fig. 2b.

direction. At $\dot{\gamma} \cong 3 \times 10^{-3}$, tumbling becomes less gradient intense and occurs less frequently, but the tilting becomes more pronounced as fluctuations around the axis decrease. See also Supplementary Movies 7–8.

During the inflation phase: Before the anomaly maximum of G_{yy}, at $\dot{\gamma} \cong 8 \times 10^{-3}$, there are rare tumbling events as the ring starts to stabilise and open. Less fluctuations are visible. See also Supplementary Movies 9–10.

In the fully inflated regime: At $\dot{\gamma} \cong 1.5 \times 10^{-2}$, the anomaly reaches its peak. The polymer is aligned with the tilting axis and quite stable. Tumbling becomes extremely rare. At $\dot{\gamma} \cong 2 \times 10^{-2}$, the polymer does not tumble but looks almost rigid. See also Supplementary Movies 11–12.

Beyond inflation: For values $\dot{\gamma} \gtrsim 10^{-1}$, the tilt angle of the rigid ring gets progressively smaller. Tumbling events resume as the polymer aligns itself very closely to the x axis. See also Supplementary Movies 13–14.

During the inflation phase and all the way into the fully inflated configuration, a particular kind of tank-treading (TT) motion shows up in lieu of the suppressed tumbling. Contrary to the usual shear-induced TT in which the rotation axis lies parallel to the vorticity direction, here we have fluctuation-induced rigid rotations of the inflated molecule around an axis lying in the flow-gradient direction perpendicular to its tilt, i.e., almost parallel to the gradient direction since θ is small.

To visualise the contribution of the solvent, in conjunction with the closed polymer topology, to this behaviour, we first compare the flow profiles established in the flow–vorticity plane around the polymer's centre of mass for contour lengths $N = 100$ and $N = 200$ as shown in Fig. 3. Additional flow fields are shown in Supplementary Figs. 1, 2. Qualitatively, the established flow fields are similar, but at the same shear rates, the $N = 200$-ring experiences a stronger backflow, and the shape and position of the horseshoe are more visible in the flow profile. At the maximum of the anomaly on G_{yy} at around $\dot{\gamma} = 2 \times 10^{-2}$ (Fig. 1c), Fig. 3d shows a clearly established backflow profile, while the same cannot be said about the $N = 100$ ring at the same shear rate (Fig. 3a).

The transition to the inflated phase is closely related to the pattern of inter-monomer and hydrodynamic forces acting on the ring. Due to the development of a strongly stretched configuration, the former are exclusively elastic forces from the tethering (FENE) potentials between successive beads; contacts between monomers are extremely rare and the excluded volume interactions are inactive there. In Fig. 4a–c, we show the gradient-direction component of the inter-monomer force, $\bar{\mathbf{F}}_{m,y}$, as a function of the distance from the centre of mass for three different ring sizes and shear rates slightly below, slightly above and well above the crossover value $\dot{\gamma}_\times$ for each length. The observed force is always directed towards the centre of mass and is the strongest near the latter, where also the tension along the chain is the strongest, as can be seen in Fig. 4d. The gradient component forces features, for the two longest rings that undergo an inflation phase, a striking development as $\dot{\gamma}_\times$ is crossed: a prolonged region along the ring where $\bar{\mathbf{F}}_{m,y} \cong 0$ develops, which arises from the emergence of portions of the ring that remain essentially horizontal, so that no y component of the force results, see Fig. 6c. At the same time, the fluid streams also smoothly and almost horizontally along these portions, see Supplementary Fig. 2e, h, so that the ring is at stable equilibrium there. As we move to higher shear rates, this region gets smaller, and there are stronger forces acting on beads far away from the centre of mass. The stretching associated with the onset of the inflation phase is clearly seen in the significant growth of the average bond length $\langle b\rangle$ with the shear rate, shown in Fig. 4e. The degree of stretching for a given shear rate grows with N, in agreement with theoretical considerations on the dependence of the tension blob size on these parameters to be presented in the Discussion section. At the tips of the ring, as well as close to their centres, the inter-monomer forces tend to push the beads towards the neutral plane and they are counteracted by hydrodynamic forces of the streaming solvent, which is deflected on the polymer, see Supplementary Fig. 2 and the schematic panel, Fig. 4f sketching the balance of inter-monomer and solvent-induced forces, $\bar{\mathbf{F}}_{m,y}$ and $\bar{\mathbf{F}}_{s,y}$, respectively, on the tips of the ring.

Referring to the typical shear rates $\dot{\gamma}_1$, $\dot{\gamma}_2$ and $\dot{\gamma}_3$ in Fig. 4a–c, we propose the following response patterns to shear for rings of sufficiently large contour length. As shear rate increases from equilibrium, ring polymers start swelling first in flow direction and align with an axis in the flow-gradient plane. They fluctuate around this axis, and occasionally experience tumbling because of sufficiently strong fluctuations of the horseshoe regions. Approaching $\dot{\gamma}_1$, tumbling becomes enhanced and the knot starts to experience backflow from the horseshoe regions. Near $\dot{\gamma}_2$, tumbling is almost completely suppressed. The backflow causes so much tension along the ring that fluctuations are suppressed. For tumbling to occur, an entire section of the ring would have to angle towards the centre-of-mass plane. At the same time, during the transition between $\dot{\gamma}_1$ and $\dot{\gamma}_2$, the alignment angle is almost constant, so the extension of the ring in gradient direction, and by extension the strength of shear and backflow, scales proportional to shear rate. Eventually, transitioning from $\dot{\gamma}_2$ to $\dot{\gamma}_3$, the sheared solvent flows powerfully enough to push the ring into the flow–vorticity plane, and the hydrostatic bubble becomes less and less pronounced. In contrast, rings with low contour length never experience a point where fluctuations are suppressed enough to prevent tumbling, and a local maximum for G_{yy} is not observed. Additional commentary on the hydrostatic bubble is provided in Supplementary Note 1.

Collapse of all knots and localisation in space. We have also investigated and compared behaviour of knotted rings and report very similar behaviour under strong shear. The diagonal entries of the gyration tensor (Fig. 5a–c) all show the same qualitative behaviour, and across all knot topologies, and the anomaly is present for G_{yy} (Fig. 5c). The stabilisation of the alignment angle is common across all topological varieties as well (Fig. 5d), and we conclude that shapewise, it is justified to talk about a generic behaviour of ring-shaped topologies rather than just of the 0_1 ring.

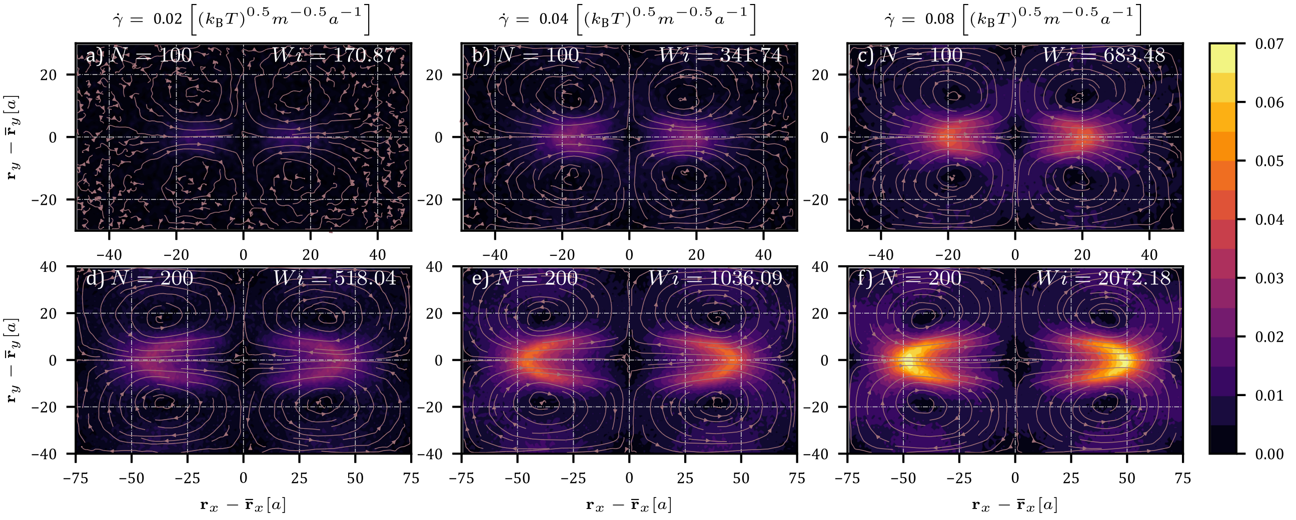

Fig. 3 Flow fields in the flow-vorticity plane centred around the centre of mass $\bar{\mathrm{r}}$ of a 0_1 ring. The colour map encodes velocity magnitudes in units of $[(k_BT)^{0.5}\ m^{-0.5}]$. Left to right: increasing shear rates $\dot{\gamma} = 0.02, 0.04, 0.08\ [(k_BT)^{0.5}m^{-0.5}a^{-1}]$. Top to bottom: increasing contour length $N = 100$, 200. Direct comparison between equal shear rates shows that backflow is significantly more pronounced at $N = 200$.

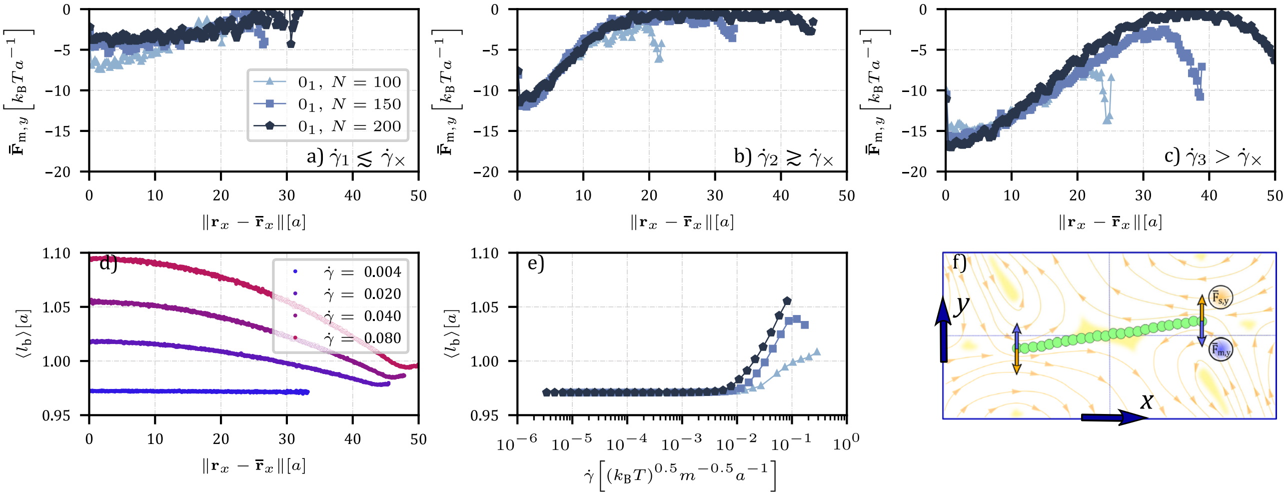

Fig. 4 Inter-monomer forces and bond extension along the ring. a–c Gradient-direction component of force on beads, averaged in intervals along the flow axis and measured relative to the centre of mass. A negative sign signifies a pull towards the centre of mass. Shear rate increases from (**a**) to (**c**). **a** At $\dot{\gamma}_1 = [0.020, 0.006, 0.003]$ for $N = [100, 150, 200]$, G_{yy} first takes on the value of its local maximum. This has to be estimated for $N = 100$, where monotony is maintained. **b** At $\dot{\gamma}_2 = [0.040, 0.020, 0.018]$ for $N = [100, 150, 200]$, G_{yy} reaches its local maximum. **c** At $\dot{\gamma}_3 = [0.286, 0.171, 0.082]$ for $N = [100, 150, 200]$, G_{yy} has become substantially smaller than it was at the local maximum. **d** Bond extension of the $N = 200$-ring along the flow axis. 0.97[a] is the average for equilibrium with the parameters given in the simulation. **e** Average bond extension increasing with shear rate. **f** A schematic view of the inflated ring on the flow-gradient plane alongside with the polymer-induced velocity deviation field of the solvent from its undisturbed profile $\mathbf{v}_s(\mathbf{r})$ in the absence of the polymer, extracted from Supplementary Fig. 2.

All knotted sections are pulled tight (Fig. 5e) and stay small for the remainder of the simulation, essentially filling the role of a particularly bulky bead. This bead-like knotted section has a preferred position on the ring, although this constraint might be lifted as the ring aligns more and more with the flow axis. Below this threshold, however, the knot tends to be located on the horseshoe region of the ring (Fig. 5f), and as tumbling is suppressed, only has tank treading as a possible way to move swiftly. In this sense, the knotted section acts as a stabilisation anchor for the ring, which already experiences a strongly suppressed, fluctuating form of tank treading rather than a pronounced one[22]. The knotted section adds to this effect. When the knotted section does move, and when it manages to leave the horseshoe region, it very quickly tank-treads to the opposite horseshoe region to stabilise there again. Supplementary Movies 15–18 of knotted rings under shear are provided for visualisation purposes; simulation snapshots of knotted and unknotted rings under shear are shown in Supplementary Figs. 3–9. Developments of knotted section size with time for a select few knot topologies, contour lengths and Weissenberg numbers (with and without HI) are shown in Supplementary Figure 10. Additional commentary on the behaviour of knots is provided in Supplementary Note 2.

Discussion

To understand the physical mechanism behind the transition from the tumbling to the inflation phase and to make quantitative predictions about its occurrence, we need to properly understand the interplay between polymer orientation in the shear field and

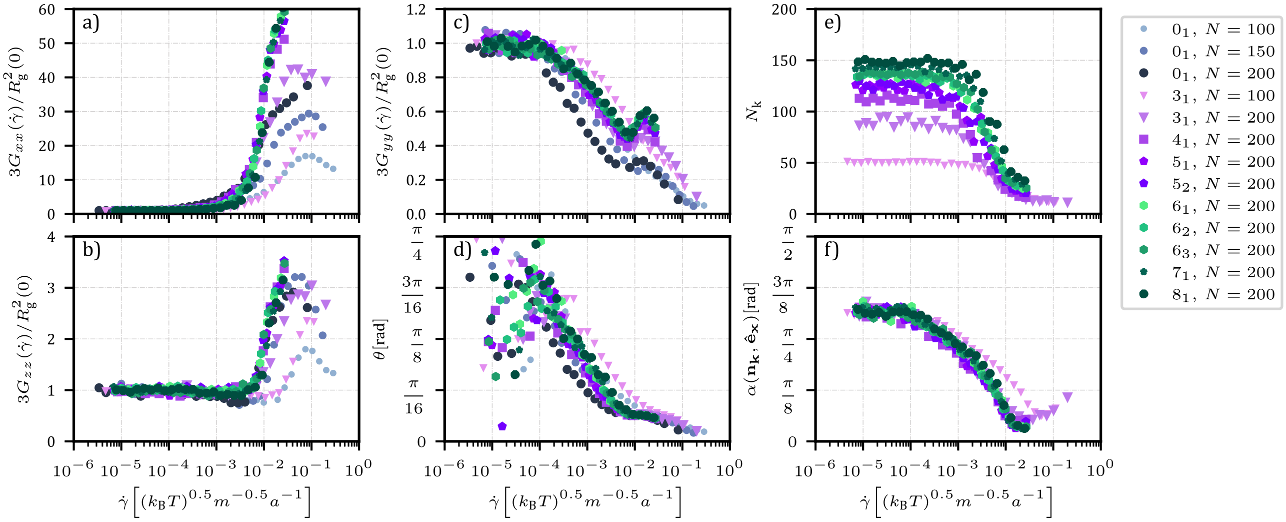

Fig. 5 Shape and orientation of knotted ring topologies under increasing shear rate. a G_{xx} (flow), **b** G_{zz} (vorticity), **c** G_{yy} (gradient), **d** alignment angle θ, **e** the number of beads on the knotted section, N_k. **f** Angle α between vector $\mathbf{n_k}$ from the ring's to the knotted section's centre of mass and axis vector $\hat{\mathbf{x}}$, under strong shear, all knot topologies behave almost exactly like a ring with the same contour length N. Different colours correspond to different knot types, as indicated in the legend.

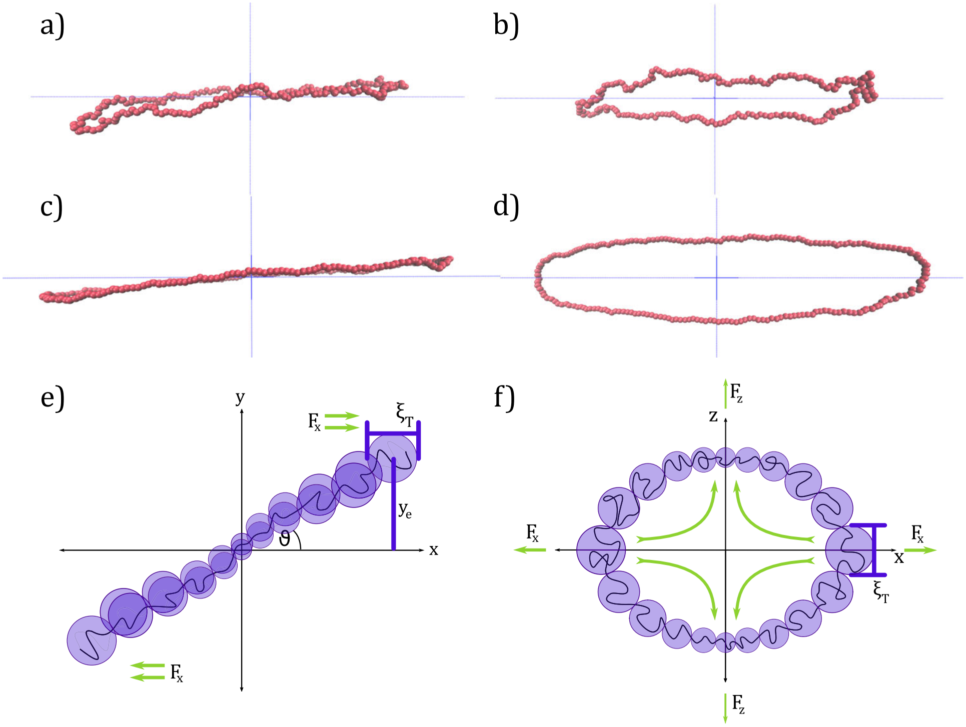

Fig. 6 Snapshots and sketches of a sheared ring. a Simulation snapshot of $N = 200$-ring at the onset of the inflation phase, on the flow-gradient (x-y) plane. $Wi =$ 145.06, $\dot{\gamma} = 5.6 \times 10^{-3}[(k_BT)^{0.5}m^{-0.5}a^{-1}]$. **b** As **a**, on the flow-vorticity (x-z) plane. **c** Stretched and inflated configuration on the flow-gradient (x-y) plane. $Wi = 543.95$, $\dot{\gamma} = 2.1 \times 10^{-2}$ $[(k_BT)^{0.5}m^{-0.5}a^{-1}]$. **d** As **c**, on the flow-vorticity (x-z) plane. In all four panels **a**–**d**, the solid scale bar in the centre extends to 5 σ in all directions. **e** Viewed projected on the flow-gradient (x-y) plane, the ring is rendered as a succession of blobs, the largest of which is located at the tips and has size ξ_T. The elevation of the tip over the neutral (flow-vorticity) plane is y_e, and the tilt angle is θ. **f** Viewed projected onto the flow-vorticity (x-z) plane, the ring has an oval shape and it is stretched outwards in all directions due to the backflow of solvent (denoted by the curved green arrows), reflected at the two horseshoe-shaped regions at the tips.

the hydrodynamic forces imposed on it by the solvent. In Fig. 6, we show simulation snapshots of the ring at the beginning and the end of the inflation phase, panels 6a–d, accompanied by a schematic blob picture in panels 6e and f that facilitates a theoretical treatment of the processes at hand.

In Fig. 6e, the average tilt angle θ of the ring is shown, subtended by the vector corresponding to the largest eigenvalue of the gyration tensor and the flow axis, alongside with the elevation y_e of the tip at the horseshoe region of the ring. In Fig. 6f, a top view of the ring is shown, featuring an open ellipsoidal shape characteristic of the swelling in the vorticity direction, caused by the backflow of the solvent reflected in the horseshoe regions[22]. Due to the form of the flow pattern, shown in Fig. 3 and sketched in Fig. 6f by the curved green arrows, the whole ring experiences an outward-pointing inflation force (akin to the pressure in the interior of an elastic bubble), and thus it can be thought of as a succession of tension blobs. The largest of these, having size ξ_{T}, is located at the tips of the ring. A necessary condition for tumbling is

$$\xi_{\mathrm{T}} \geq y_{\mathrm{e}}, \tag{3}$$

so that parts of the upper (lower) tip of the ring can be found below (above) the neutral plane and carried to the opposite direction by the streaming fluid. Accordingly, we need to estimate the dependence of y_{e} and ξ_{T} on the shear rate $\dot{\gamma}$.

From geometrical considerations, we have

$$y_{\mathrm{e}} \cong \sqrt{G_{xx}} \tan\theta \cong \sqrt{G_{xx}}\, \theta, \tag{4}$$

for small values of θ, typical of the transition to the inflation phase. The flow-direction component of the gyration tensor, G_{xx}, scales in the tumbling regime as $G_{xx}(\dot{\gamma})/G_{xx}(0) \sim Wi^{0.6}$[22,57]. Keeping in mind that $G_{xx}(0) \propto R_{\mathrm{g}}^2(0) \sim N^{2\nu}$ with the Flory exponent $\nu \cong 0.588$, the above considerations yield

$$\sqrt{G_{xx}} \sim \dot{\gamma}^{0.3} \tau_{\mathrm{R}}^{0.3}\ N^{\nu}. \tag{5}$$

The dependence of the tilt angle θ on the shear rate can be extracted from the scaling of the orientational resistance $m_{\mathrm{G}} = Wi \tan(2\theta) \cong 2\theta\ Wi$ on the Weissenberg number: $m_{\mathrm{G}} \sim Wi^{0.6}$, implying

$$\theta \sim \dot{\gamma}^{-0.4}\ \tau_{\mathrm{R}}{}^{-0.4}. \tag{6}$$

Combining Eqs. (4), (5) and (6) above, together with the power law $\tau_{\mathrm{R}} \sim N^{3\nu}$ for the dependence of the longest relaxation time of the polymer on N, we obtain

$$y_{\mathrm{e}} \sim \dot{\gamma}^{-0.1}\ N^{0.4}, \tag{7}$$

where the approximation $0.7\,\nu \cong 0.4$ has been employed.

The magnitude of the inflating force F that stretches the ring and gives rise to the tension blobs is set by the streaming velocity of the solvent at the point of the highest elevation y_{e}, and it scales as $F \sim \dot{\gamma}\, y_{\mathrm{e}}$. The ensuing tension blob size scales as $\xi_{\mathrm{T}} \sim k_{\mathrm{B}}T/F \sim \dot{\gamma}^{-1} y_{\mathrm{e}}^{-1}$, resulting, together with Eq. (7), in

$$\xi_{\mathrm{T}} \sim \dot{\gamma}^{-0.9}\ N^{-0.4}. \tag{8}$$

Evidently, ξ_{T} decreases with the shear rate $\dot{\gamma}$ much faster than y_{e}, so that beyond a crossover shear rate $\dot{\gamma}_{\times}$, the inequality (3) cannot be fulfilled and tumbling strongly suppressed the ring transitioning into the inflation phase. Putting together Eqs. (3), (7) and (8), we find the dependence of $\dot{\gamma}_{\times}$ with N to follow a simple power law

$$\dot{\gamma}_{\times} \sim \frac{k_{\mathrm{B}}T}{\eta\sigma^3} N^{-1}, \tag{9}$$

where we have reintroduced in the prefactor the quantities entering in the expressions of y_{e} and F to obtain the full dependence on the temperature, solvent viscosity and monomer size as well.

There is a striking comparison that can be made here with the case of suspensions of colloidal particles of size d under shear. There, the Peclet number Pe, which scales as

$$Pe \sim \frac{\eta\dot{\gamma}d^3}{k_{\mathrm{B}}T}, \tag{10}$$

expresses the typical ratio of timescales for Brownian and shear-induced motions[58]. The Brownian character of the motion dominates for $Pe \lesssim 1$, whereas shear takes over for $Pe > 1$ and the particles become fully non-Brownian for $Pe \gg 1$. Accordingly, and defining a crossover value $Pe_{\times} = 1$ between the two regimes, this translates, for colloidal particles, into a crossover shear rate

$$\dot{\gamma}_{\times} \sim \frac{k_{\mathrm{B}}T}{\eta d^3}. \tag{11}$$

Comparing Eqs. (9) and (11), we see that the former is fully consistent with the interpretation and the physical picture of the inflated, stressed ring as a succession of N particles of size σ held together by essentially rigid connections. The fact that it has been derived independently, using scaling arguments from polymer theory, and at the same time it turns out to deliver a physically consistent picture of an inflated polymer as a rigid, non-Brownian colloid, offers additional corroboration of its validity.

Using the typical orders of magnitude, $\eta \cong 10$ and $N \cong 10^2$ employed in this work, we obtain $\dot{\gamma}_{\times} \cong 10^{-3}$, in satisfactory agreement with the results in Table 1. Though we have only simulated rings with three different N values, the results shown in Fig. 2b and summarised in Table 1 also support the above power-law prediction. Moreover, translating the crossover shear rate into a crossover Weissenberg number $Wi_{\times} = \dot{\gamma}_{\times}\tau_{\mathrm{R}}$ and using the scaling $\tau_{\mathrm{R}} \sim N^{3\nu}$, we obtain $Wi_{\times} \sim N^{0.76}$. Accordingly, employing ring polymers of high N guarantees that the condition of lying in the strongly nonlinear regime, $Wi_{\times} \gg 1$, is satisfied. At the same time, increasing N lowers the value $\dot{\gamma}_{\times}$ of the shear rate at which the transition to the inflation phase will take place, therefore making the phenomenon more easily observable experimentally.

Once the rings enter their inflation phase, the orientational resistance scales as $m_{\mathrm{G}} \sim Wi$, directly implying $\theta \sim Wi^0$: the orientation angle remains constant during this phase and the ring simply fully unfolds until the tension blob reaches the monomer size. Thereafter, it behaves as a rigid, non-Brownian object for which thermal fluctuations play no role. The highest elevation scales as $y_{\mathrm{e}} \sim N$ [cf. Eq. (7)] and the hydrodynamic force on the monomers scales, accordingly, as $F \sim \dot{\gamma}\ N$, cf. $F \sim \dot{\gamma}^{0.9}\ N^{0.4}$ in the tumbling regime.

Within the inflated phase and at the stretched limit, where the blob size has been reduced down to the monomer size $\xi_{\mathrm{T}} \sim \sigma = 1$, the relevant Brownian force fluctuations are not any more included into the blob picture presented above, but they need to be considered on a single-monomer level. Close to the tips, the ring has at this phase a locally horizontal configuration running along the vorticity axis, with stretched FENE bonds of typical length $r_0 = \langle b \rangle \cong 1$ in the inflated phase, see Fig. 4d, e. The frequency of transversal oscillations of the monomers along the y axis is given by

$$\omega_{\mathrm{tr}}^2 = \frac{2k}{m}\left(1 - \frac{r_0^2}{R_0^2}\right)^{-1}, \tag{12}$$

with $k = 30$ $[k_{\mathrm{B}}T\sigma^{-2}]$ and $R_0 = 1.5\sigma$ being the spring constant and maximum extension of the FENE springs, respectively. At the same time, the monomers are subject to random, Brownian forces due to collisions with the solvent. If the tip monomers cross the $(x{-}z)$ plane as they are kicked by random forces away from their equilibrium positions at $\pm y_{\mathrm{e}}$ (at $x > 0$ or $x < 0$, respectively), tumbling events can be triggered. Setting $Y(t) = y(t) \mp y_{\mathrm{e}}$, the motion of the monomers along the y direction, can be described by the Langevin equation

$$m\ddot{Y}(t) + \zeta\dot{Y}(t) + \frac{m\omega_{\mathrm{tr}}^2 y_{\mathrm{e}}}{\pi}\sin(\pi Y(t)/y_{\mathrm{e}}) = \Gamma(t), \tag{13}$$

with the friction constant ζ and the random noise $\Gamma(t)$ satisfying the conditions

$$\langle\Gamma(t)\rangle = 0; \tag{14}$$

$$\langle\Gamma(t)\Gamma(t')\rangle = 2\zeta k_{\mathrm{B}}T\delta(t - t'). \tag{15}$$

Equation (13) is suitable for the description of the dynamics of the variable $y(t)$, as it yields a harmonic restoring force of the form $m\omega_{\mathrm{tr}}^2(y(t) \mp y_{\mathrm{e}})$ for small deviations of $y(t)$ around $\pm y_{\mathrm{e}}$ (i.e., $Y(t) \cong 0$) and a vanishing restoring force at $y = 0$ (i.e., $Y = \mp y_{\mathrm{e}}$).

Quantitative results about the statistical properties of the fluctuating quantity $Y(t)$ are discussed extensively in ref. [59]. Following the notation there, we define new variables as follows:

$$X = \frac{\pi Y}{y_{\mathrm{e}}}; \tag{16}$$

$$d = \frac{m\omega_{\mathrm{tr}}^2 y_{\mathrm{e}}^2}{\pi^2}; \tag{17}$$

$$\Theta = k_{\mathrm{B}}T, \tag{18}$$

so that—f_{int}, the third term on the left-hand side of Eq. (13), arises from a potential $u(X) = -d\cos(X)$ as $-f_{\mathrm{int}} = (\pi/y_{\mathrm{e}})u'(X)$. The properties of the probability distribution function $W(X)$ of the variable X in the high-friction limit are discussed in detail in Chapter 11 of ref. [59]. As physically expected, a key role is played by the ratio Θ/d between the thermal and elastic energies. Using the above expressions, we obtain

$$\frac{\Theta}{d} = \frac{\pi^2 k_{\mathrm{B}}T}{2ky_{\mathrm{e}}^2(\dot{\gamma})}\left[1 - \frac{r_0^2(\dot{\gamma})}{R_0^2}\right]. \tag{19}$$

We have denoted explicitly the dependence of the quantities r_0 and y_{e} on $\dot{\gamma}$, since the shear rate on the one hand stretches the bonds and on the other it tilts the ring towards the flow axis. Concomitantly, it induces two opposing trends on the ratio Θ/d, as is clear from Eq. (19). Using the values $k_{\mathrm{B}}T = 1$, $k = 30$, and $R_0 = 1.5$ of the polymer model, together with the typical values $r_0 \cong 1$ and $y_{\mathrm{e}} \cong 5$ at the stretched phase (see Fig. 6a–d), we obtain

$$\Theta/d \cong 0.004, \tag{20}$$

which is small, rendering the probability distribution function $W(X)$ strongly peaked around $X = 0$, i.e., $y(t)$ is strongly peaked around y_{e}, see e.g., Fig. 11.9 of ref. [59]. This finding is in full agreement with our simulation results showing stable polymer conformations with small fluctuations of the monomers of the stretched ring around their equilibrium values and strong suppression (even absence within the simulation time window) of tumbling events. Note that in ref. [59], in addition to interactions and Brownian forces, a constant external drift force F is considered, the effect of which is to shift the peak of the distribution function $W(X)$ at $X = F/d$ for small Θ/d values. Here, $F = 0$.

The above arguments demonstrate that there is a regime in which the polymer is stretched and the elevation y_{e} is sufficiently high, such that Brownian fluctuations hardly have a chance of pushing the tip monomer below (above, for the opposite side) the neutral plane and causing tumbling. Following up on the above considerations, the question then arises what happens to the rigidified polymer as $\dot{\gamma}$ further grows, and after the inflation phase during which the polymer orientation remains fixed, the rigid object starts tilting again more towards the flow axis. As y_{e} then becomes smaller, Eq. (19) implies that the ratio Θ/d will grow and tumbling will resume. The simulations performed with time step $h = 0.05$ allow us to reach higher Weissenberg numbers, and indeed, the onset of re-entrant tumbling has been seen there. We provide Supplementary Movies 13–14 showing the above pattern in the post-inflation tumbling regime.

The swelling of rings in vorticity direction is exclusive to their closed structure and their transition to the stretched, inflated configuration is size specific. Accordingly, we surmise that this property could be employed in a simple microfluidic device to enhance separation of large and small rings in a mixture under Poiseuille flow. Indeed, the latter creates a parabolic velocity profile for the Newtonian solvent in which the mixture is suspended, causing thereby a position-varying shear rate $\dot{\gamma}(y)$ across the gradient direction y. This local shear rate has a maximum close to the walls and vanishes in the middle of the channel. Large rings exposed to high shear close to the walls will inflate and stretch, orient themselves almost parallel to the wall and thus be subject to both steric constraints with one another and strong lift forces from the wall. It is thus natural to expect that they will migrate towards the centre of the channel, and displacing from there smaller rings that will be pushed towards the walls. In this way, a flow-induced size separation via focusing of the large rings in the middle can be achieved. The same scenario has been put forward for mixtures of linear chains and rings in Poiseuille flow with explicit walls, and it has been recently confirmed by employing MPCD simulations for dilute and semidilute solutions that such a mechanism indeed plays an important role in focusing the rings towards the channel centre, while linear chains migrate to the vicinity of the walls[60].

We have shown that ring polymers in the presence of fully developed hydrodynamic interactions behave remarkably different from chains, stars, branched or cross-linked polymers under pure, steady shear alone. They show a unique inflation in the vorticity direction because of a well-established backflow, which highlights the importance of carefully realised hydrodynamics when dealing with such closed topologies. For rings with high contour length, an interplay between alignment at an angle to the flow axis and the backflow causes the ring to self-stabilise in gradient direction and leads to a strong suppression of tumbling and a suppression of tank treading. The entire object looks and behaves more like a rigid ring in this configuration, and it behaves in this way even in the presence of complex knots along its backbone. Contrary to recently reported polymer-stretched states that appear at ultrahigh shear rates, require nonlinear flow profiles and also depend on box shapes and sizes[61], the inflation phase reported here appears at moderate shear rates, corresponding to $Wi \cong 100$, and it is present for linear velocity profiles as well as robust with respect to changing the simulation box size. On the basis of these phenomena, we suggest a potential microfluidic filter to separate rings from chains, or rings of different sizes from each other[60]. As a knotted section on a sufficiently long ring has very sharp tank-treading-like transitions from one side of an open ring to another, we also envision that fluorescence techniques could be used to detect the presence of such a tight knot on a ring.

Although this work was focused on single-molecule numerical experiments, future extensions should focus on the effects of shear and of the ring-stretching transition to the rheological behaviour of dilute or semidilute ring polymer mixtures, as well as on the interplay between inflation and polymer rigidity. The former should be directly comparable with rheology experiments on ring polymer solutions, whereas the latter system can be realised by employing, e.g., short DNA rings. Work along these lines is currently under way.

Methods

Multi-particle collision dynamics. The MPCD technique[53,62] allows us to simulate a particle-based, mesoscopic solvent with fully developed hydrodynamic interactions. MPCD features two alternating steps: streaming, where particles propagate, and collision, where one separates the system into smaller cells of length a and computes the centre-of-mass velocity $\mathbf{v}_{\mathrm{CM}}$ in each, performing a random rotation of all deviations of the cell–particle velocity vectors from the latter, and adding it back to produce new, post-collision velocities. Because our simulations involve shear, the system would continuously heat up by viscous heating. To prevent this, we apply a cell-level Maxwellian thermostat[62]. We employ the usual choice of parameters[22,62] with a collision cell length a as a unit of length and rotation angle $\chi = 130°$. All solvent particles are assigned a mass of m, serving as the unit of mass. We set the average number of solvent particles per cell as $\langle N_{\mathrm{c}}\rangle = 10$ and the MPCD collision time step $h = 0.1$ $[(k_{\mathrm{B}}T)^{-0.5}m^{0.5}a]$, with k_{B} being Boltzmann's constant and T the absolute temperature. With our choice of parameters, the solvent dynamic viscosity η yields the value $\eta = \eta_{\mathrm{kin}} + \eta_{\mathrm{col}} \cong 8.70\ [(k_{\mathrm{B}}T)^{0.5} m^{0.5} a^{-2}]$, where η_{kin} and η_{col} are the kinetic and collisional contributions to the viscosity[62]. In addition, we have tested the influence of the time step h for the $N = 150$-ring at $h = 0.05$ and present these results in Fig. 1a–f. The ring in a simulation with such a halved time step shows the same behaviour. The solvent in these simulations has an altered viscosity of $\eta \cong 16.67\ [(k_{\mathrm{B}}T)^{0.5} m^{0.5} a^{-2}]$ in accordance with values quoted in the literature[62]. We also performed simulations of selected chains and rings in which HI has been switched off[22,51,52]. The results obtained from those are summarised in Fig. 1g–i.

Lees–Edwards boundary conditions. The shear in our simulation is implemented by Lees–Edwards boundary conditions[54] with a prescribed shear rate $\dot{\gamma}$. With $\hat{\mathbf{x}}, \hat{\mathbf{y}}$ and $\hat{\mathbf{z}}$ being the flow, gradient and vorticity directions, respectively, these boundary conditions establish the velocity profile of planar Couette flow of the solvent in the absence of a polymer as $\mathbf{v}_{\mathrm{s}}(\mathbf{r}) = \dot{\gamma} y \hat{\mathbf{x}}$.

Molecular dynamics. We employ the Kremer–Grest bead–spring model[63,64] to investigate the properties of a fully flexible polymer. We employ $\epsilon = k_{\mathrm{B}}T = 1.0$ and $\sigma = a = 1.0$ as units of energy and length from the Weaks–Chandler–Andersen (WCA) potential, respectively. We set the parameters for the FENE potential to $k = 30\ \epsilon\sigma^{-2}$ and $R_0 = 1.5\ \sigma$. With these settings, the expected bond length $\langle l_{\mathrm{b}} \rangle = 0.965\ \sigma$. Velocity-Verlet[65] with a time step $\delta t = h/100 = 0.001\ [(k_{\mathrm{B}}T)^{-0.5} m^{0.5} a]$ was used to solve the MD equations of motion. This algorithm is easily coupled to MPCD by setting the mass of each monomer $M = m\langle N_{\mathrm{c}} \rangle$ and having the monomers participate in the collision step[22,62]. We have chosen to use the Alexander Polynomial[66] to detect and the minimum-closure scheme to localise[67] the knotted section on all simulated rings carrying knots. Simulating the various polymers in equilibrium allows us to determine as well their longest relaxation time τ_{R}, from which the Weissenberg number[68] $Wi = \dot{\gamma}\tau_{\mathrm{R}}$ can be extracted for different contour lengths. A summary of the relaxation times is given in Supplementary Table 1.

GPU and system size. Our code has been written with CUDA/C++[69] to run in parallel on a GPU cluster[70]. This enabled more extensive simulations over a longer period of time to study flow profiles in detail. We also increased the simulation box volume to minimise residual effects by system size limitations. Our box sizes were $V = (100 \times 60 \times 60)a^3$ for a number of monomers $N = 100$ and $V = (150 \times 80 \times 80)a^3$ for $N = 150$ and $N = 200$. We have tested the influence of the box size by running a simulation with $V = (200 \times 120 \times 120)a^3$ for $N = 150$, which consistently reproduced the same behaviour. Boxes are elongated in the flow direction $\hat{\mathbf{x}}$ to accommodate the stretched polymer there, and quadratic in the gradient- and vorticity directions $\hat{\mathbf{y}}$ and $\hat{\mathbf{z}}$. Our findings on the polymer conformation do not depend on the box size although the details of the solvent flow show signatures of finite box sizes, such as vortices away from the region occupied by the polymer.

Image processing. All data have been visualised using `matplotlib`, a Python library. Figure 4f and Fig. 6e, f were created with the Inkscape software. Snapshots and videos were created using VMD[71].

Data availability

The relevant data sets generated during and/or analysed during this study are available from the corresponding author on reasonable request.

Code availability

The `CUDA/C++` code employed for generating the data in this study is available from the corresponding author on reasonable request.

Received: 16 September 2019; Accepted: 17 December 2019;
Published online: 04 February 2020

References

1. Grosberg, A. & Nechaev, S. Polymer topology. *Adv. Pol. Sci.* **106**, 1–29 (1993).
2. Frank-Kamenetskii, M. D., Lukashin, A. V. & Vologodskii, A. V. Statistical mechanics and topology of polymer chains. *Nature* **258**, 398–402 (1975).
3. Katritch, V. et al. Geometry and physics of knots. *Nature* **384**, 142–145 (1996).
4. Micheletti, C., Marenduzzo, D. & Orlandini, E. Polymers with spatial or topological constraints: Theoretical and computational results. *Phys. Rep.* **504**, 1–73 (2011).
5. Kapnistos, M. et al. Unexpected power-law stress relaxation of entangled ring polymers. *Nat. Mater.* **7**, 997–1002 (2008).
6. Huang, Q. et al. Unexpected stretching of entangled ring macromolecules. *Phys. Rev. Lett.* **122**, 208001 (2019).
7. Moore, N. T., Lua, R. C. & Grosberg, A. Y. Topologically driven swelling of a polymer loop. *PNAS* **101**, 13431–13435 (2004).
8. Bohn, M. & Heermann, D. W. Topological Interactions between ring polymers: implications for chromatin loops. *J. Chem. Phys.* **132**, 044904 (2010).
9. Narros, A., Moreno, A. J. & Likos, C. N. Influence of topology on effective potentials: coarse-graining ring polymers. *Soft Matter* **6**, 2435–2441 (2010).
10. Vettorel, T., Grosberg, A. Y. & Kremer, K. Statistics of polymer rings in the melt: a numerical simulation study. *Phys. Biol.* **6**, 025013 (2009).
11. Halverson, J. D., Lee, W. B., Grest, G. S., Grosberg, A. Y. & Kremer, K. Molecular dynamics simulation study of nonconcatenated ring polymers in a melt. I. Statics. *J. Chem. Phys.* **134**, 204904 (2011).
12. Sakaue, T. Ring Polymers in melts and solutions: scaling and crossover. *Phys. Rev. Lett.* **106**, 167802 (2011).
13. Grosberg, A. Y. Annealed lattice animal model and Flory theory for the melt of non-concatenated rings: towards the physics of crumpling. *Soft Matter* **10**, 560–565 (2014).
14. Halverson, J. D., Smrek, J., Kremer, K. & Grosberg, A. Y. From a melt of rings to chromosome territories: the role of topological constraints in genome folding. *Rep. Progr. Phys.* **77**, 022601 (2014).
15. Halverson, J. D., Grest, G. S., Grosberg, A. Y. & Kremer, K. Rheology of ring polymer melts: from linear contaminants to ring-linear blends. *Phys. Rev. Lett.* **108**, 038301 (2012).
16. Pasquino, R. et al. Viscosity of ring polymer melts. *ACS Macro Lett.* **2**, 874–878 (2013).
17. Goossen, S. et al. Influence of the solvent quality on ring polymer dimensions. *Macromolecules* **48**, 1598–1605 (2015).
18. Michieletto, D. & Turner, M. S. A topologically driven glass in ring polymers. *Proc. Natl Acad. Sci. USA* **113**, 5195–5200 (2016).
19. Michieletto, D., Nahali, N. & Rosa, A. Glassiness and heterogeneous dynamics in dense solutions of ring polymers. *Phys. Rev. Lett.* **119**, 197801 (2017).
20. Li, Y. et al. When ends meet: circular DNA stretches differently in elongational flows. *Macromolecules* **48**, 5997–6001 (2015).
21. Hsiao, K.-W., Schroeder, C. M. & Sing, C. E. Ring polymer dynamics are governed by a coupling between architecture and hydrodynamic interactions. *Macromolecules* **49**, 1961–1971 (2016).
22. Liebetreu, M., Ripoll, M. & Likos, C. N. Trefoil knot hydrodynamic delocalization on sheared ring polymers. *ACS Macro Lett.* **7**, 447–452 (2018).
23. Young, C. D., Qian, J. R., Marvin, M. & Sing, C. E. Ring polymer dynamics and tumbling-stretch transitions in planar mixed flows. *Phys. Rev. E* **99**, 062502 (2019).
24. Koniaris, K. & Muthukumar, M. Knottedness in ring polymers. *Phys. Rev. Lett.* **66**, 2211–2214 (1991).
25. Wasserman, S. A. & Cozzarelli, N. R. Biochemical topology: applications to DNA recombination and replication. *Science* **232**, 951–960 (1986).
26. Rybenkov, V. V., Cozzarelli, N. R. & Vologodskii, A. V. Probability of DNA knotting and the effective diameter of the DNA double helix. *Proc. Natl Acad. Sci. USA* **90**, 5307–5311 (1993).
27. Micheletti, C., Marenduzzo, D., Orlandini, E. & Sumners, D. W. Simulations of knotting in confined circular DNA. *Biophys. J.* **95**, 3591–3599 (2008).
28. Virnau, P., Mirny, L. A. & Kardar, M. Intricate knots in proteins: function and evolution. *PLoS Comput. Biol.* **2**, e122 (2006).
29. Sułkowska, J. I., Noel, J. K. & Onuchic, J. N. Energy landscape of knotted protein folding. *Proc. Natl Acad. Sci. USA* **109**, 17783–17788 (2012).
30. Dabrowski-Tumanski, P. & Sułkowska, J. I. Topological knots and links in proteins. *Proc. Natl Acad. Sci. USA* **114**, 3415–3420 (2017).
31. Arai, Y. et al. Tying a molecular knot with optical tweezers. *Nature* **399**, 446–448 (1999).
32. Bao, X. R., Lee, H. J. & Quake, S. R. Behavior of complex knots in single DNA Molecules. *Phys. Rev. Lett.* **91**, 265506 (2003).
33. Leigh, D., Woltering, S. L. & Fielden, S. Molecular knots. *Angew. Chem. Int. Ed.* **56**, 11166–11194 (2017).
34. Tubiana, L., Rosa, A., Fragiacomo, F. & Micheletti, C. Spontaneous knotting and unknotting of flexible linear polymers: equilibrium and kinetic aspects. *Macromolecules* **46**, 3669–3678 (2013).
35. Dai, L. & Doyle, P. S. Effects of intrachain interactions on the knot size of a polymer. *Macromolecules* **49**, 7581–7587 (2016).
36. Quake, S. R. Topological effects of knots in polymers. *Phys. Rev. Lett.* **73**, 3317–3320 (1994).
37. Dai, L., van der Maarel, J. & Doyle, P. S. Effect of nanoslit confinement on the knotting probability of circular DNA. *ACS Macro Lett.* **1**, 732–736 (2012).
38. Saitta, A. M., Soper, P. D., Wasserman, E. & Klein, M. L. Influence of a knot on the strength of a polymer strand. *Nature* **399**, 46–48 (1999).
39. Tang, J., Du, N. & Doyle, P. S. Compression and self-entanglement of single DNA molecules under uniform electric field. *Proc. Natl Acad. Sci. U.S.A* **108**, 16153–16158 (2011).
40. Poier, P., Likos, C. N. & Matthews, R. Influence of rigidity and knot complexity on the knotting of confined polymers. *Macromolecules* **47**, 3394–3400 (2014).

41. Caraglio, M., Micheletti, C. & Orlandini, E. Stretching response of knotted and unknotted polymer chains. *Phys. Rev. Lett.* **115**, 188301 (2015).
42. Klotz, A. R., Soh, B. W. & Doyle, P. S. Motion of knots in DNA stretched by elongational fields. *Phys. Rev. Lett.* **120**, 188003 (2018).
43. Gruziel, M. et al. Periodic motion of sedimenting flexible knots. *Phys. Rev. Lett.* **121**, 127801 (2018).
44. Ripoll, M., Winkler, R. G. & Gompper, G. Star polymers in shear flow. *Phys. Rev. Lett.* **96**, 188302 (2006).
45. Huang, C.-C., Winkler, R. G., Sutmann, G. & Gompper, G. Semidilute polymer solutions at equilibrium and under shear flow. *Macromolecules* **43**, 10107–10116 (2010).
46. Nikoubashman, A. & Likos, C. N. Branched polymers under shear. *Macromolecules* **43**, 1610–1620 (2010).
47. Formanek, M. & Moreno, A. J. Single-chain nanoparticles under homogeneous shear flow. *Macromolecules* **52**, 1821–1831 (2019).
48. Hur, J. S., Shaqfeh, E., Babcock, H. P. & Chu, S. Dynamics and configurational fluctuations of single DNA molecules in linea mixed flows. *Phys. Rev. E* **66**, 011915 (2002).
49. Woo, N. J. & Shaqfeh, E. The configurational phase transitions of flexible polymers in planar mixed flows near simple shear. *J. Chem. Phys.* **119**, 2908–2914 (2003).
50. Lang, P. S., Obermayer, B. & Frey, E. Dynamics of a semiflexible polymer or polymer ring in shear flow. *Phys. Rev. E* **89**, 022606 (2014).
51. Kikuchi, N., Gent, A. & Yeomans, J. M. Polymer collapse in the presence of hydrodynamic interactions. *Eur. Phys. J. E* **9**, 63–66 (2002).
52. Ripoll, M., Winkler, R. G. & Gompper, G. Hydrodynamic screening of star polymers in shear flow. *Eur. Phys. J. E* **23**, 349–354 (2007).
53. Malevanets, A. & Kapral, R. Mesoscopic model for solvent dynamics. *J. Chem. Phys.* **110**, 8605–8613 (1999).
54. Lees, A. W. & Edwards, S. F. The computer study of transport processes under extreme conditions. *J. Phys. C* **5**, 1921–1929 (1972).
55. Alexander, J. W. & Briggs, G. B. On types of knotted curves. *Ann. of Math* **28**, 562–586 (1926). -1927.
56. Rudnik, J. & Gaspari, G. The asphericity of random walks. *J. Phys. A: Math. Gen.* **19**, L191–L193 (1986).
57. Chen, W. et al. Conformations and dynamics of single flexible ring polymers in simple shear flow. *Polymer* **64**, 93–99 (2015).
58. Denn, M. M. & Morris, J. F. Rheology of non-Brownian suspensions. *Annu. Rev. Chem. Biomol. Eng.* **5**, 203–228 (2014).
59. Risken, H. *The Fokker-Planck Equation*. 2nd edn (Springer-Verlag, Berlin Heidelberg, 1989).
60. Weiss, L. B., Likos, C. N. & Nikoubashman, A. Spatial demixing of ring and chain polymers in pressure-driven flow. *Macromolecules* **52**, 7858–7869 (2019).
61. Wang, Z. et al. Mechanism of nonmonotonic increase in polymer size: comparison between linear and ring chains at high shear rates. *Macromolecules* **52**, 8144–8154 (2019).
62. Gompper, G., Ihle, T., Kroll, D. & Winkler, R. Multi-particle collision dynamics—a particle—based mesoscale simulation approach to the hydrodynamics of complex fluids. *Adv. Polym. Sci.* **221**, 1–91 (2008).
63. Grest, G. S. & Kremer, K. Molecular dynamics simulation for polymers in the presence of a heat bath. *Phys. Rev. A* **33**, 3628–3631 (1986).
64. Kremer, K. & Grest, G. S. Dynamics of entangled linear polymer melts: a molecular-dynamics simulation. *J. Chem. Phys.* **92**, 5057–5086 (1990).
65. Verlet, L. Computer experiments on classical fluids. I. Thermodynamical properties of Lennard-Jones molecules. *Phys. Rev.* **159**, 98–103 (1967).
66. Alexander, J. W. Topological invariants of knots and links. *Trans. Amer. Math. Soc.* **30**, 275–306 (1928).
67. Tubiana, L., Orlandini, E. & Micheletti, C. Probing the entanglement and locating knots in ring polymers: a comparative study of different Arc closure schemes. *Prog. Theor. Phys. Suppl.* **191**, 192–204 (2011).
68. White, J. L. Dynamics of viscoelastic fluids, melt fracture, and the rheology of fiber spinning. *J. Appl. Polym. Sci.* **8**, 2339–2357 (1964).
69. Nickolls, J., Buck, I., Garland, M. & Skadron, K. Scalable parallel programming with CUDA. *Queue* **6**, 40–53 (2008).
70. Westphal, E., Singh, S., Huang, C.-C., Gompper, G. & Winkler, R. Multiparticle collision dynamics: GPU accelerated particle-based mesoscale hydrodynamic simulations. *CPC* **185**, 495–503 (2014).
71. Humphrey, W., Dalke, A. & Schulten, K. VMD—visual molecular dynamics. *J. Molec. Graphics* **14**, 33–38 (1996).

Acknowledgements

The authors thank Luca Tubiana for supplying them with his LocKnot program for knot localisation, and Dimitris Vlassopoulos for a critical reading of the paper and helpful discussions. The computational results presented have been achieved in part using the Vienna Scientific Cluster (VSC). M.L. has been supported by the uni:docs Doctoral Fellowship Programme of the University of Vienna. The authors acknowledge financial support from the University of Vienna Open Access Office towards covering the publication fees of this article.

Author contributions

M.L. co-designed research, performed the simulations, analysed the results and wrote the paper. C.N.L. co-designed research, supervised the work, analysed the results and wrote the paper.

Competing interests

The authors declare no competing interests.

Additional information

Supplementary information is available for this paper at https://doi.org/10.1038/s43246-019-0006-5.

Correspondence and requests for materials should be addressed to M.L. or C.N.L.